

## All-Season Climatology and Variability of Atmospheric River Frequencies over the North Pacific

BRYAN D. MUNDHENK, ELIZABETH A. BARNES, AND ERIC D. MALONEY

*Department of Atmospheric Science, Colorado State University, Fort Collins, Colorado*

(Manuscript received 14 September 2015, in final form 6 April 2016)

### ABSTRACT

Recent work on atmospheric rivers (ARs) has led to a characterization of these impactful features as primarily cold-season phenomena. Here, an all-season analysis of AR incidence in the North Pacific basin is performed for the period spanning 1979–2014 using the NASA Modern-Era Retrospective Analysis for Research and Applications (MERRA) reanalysis dataset. An occurrence-based detection algorithm is developed and employed to identify and characterize ARs in instantaneous fields of anomalous vertically integrated water vapor transport. The all-season climatology and variability of AR frequencies due to the seasonal cycle, the El Niño–Southern Oscillation (ENSO), the Madden–Julian oscillation (MJO), and their interactions are presented based on composites of the detected features. The results highlight that ARs exist throughout the year over the North Pacific, although their preferred locations shift substantially throughout the year. This seasonal cycle manifests itself as northward and westward displacement of ARs during the Northern Hemisphere warm seasons, rather than an absolute change in the number of ARs within the domain. It is also shown that changes to the North Pacific mean-state due to ENSO and the MJO may enhance or completely offset the seasonal cycle of AR activity, but that such influences on AR frequencies vary greatly based on location.

### 1. Introduction

Atmospheric rivers (ARs) give rise to a dichotomy of both environmental and societal risks and benefits. With associated impacts ranging from torrential rainfall to replenishment of water reserves, ARs merit attention from not only scientists and operational forecasters, but also governments, resource managers, and local populations. Deservingly, ARs remain an active area of scientific research since their naming by Zhu and Newell over two decades ago (see [Zhu and Newell 1994](#); [Newell et al. 1992](#); [Newell and Zhu 1994](#); [Zhu and Newell 1998](#)) and since the widespread availability of meteorological satellite data facilitated such inquiries. ARs have been the focus of numerous articles, field campaigns, and initiatives in the recent past. Such investigations have elevated the understanding of these features and clarified their associated local dynamics, but the extent to which variations in large-scale dynamics regulate the

frequency and character of these events is not as well understood.

Atmospheric rivers are often characterized by their plumelike structure of focused tropospheric water vapor content and intense low-level winds (see [Ralph et al. 2004](#); [Gimeno et al. 2014](#), and references therein). While ARs have been found to be dynamically related to extratropical cyclones that support the synoptic-scale water vapor transport, they should be considered as distinct features with their own evolution and life cycle ([Sodemann and Stohl 2013](#)). Isolating the dominant source of moisture within individual ARs remains an active research topic. [Bao et al. \(2006\)](#), for example, categorized two types and/or life stages of ARs: those that are dominated by local moisture flux convergence and those that are more representative of long-distance, riverlike transport. After thoroughly analyzing the water vapor budget of two ARs in the North Pacific, [Cordeira et al. \(2013\)](#) described a continuum of remote and local moisture sources important in the development and maintenance of each AR's moisture flux. More recently, [Dacre et al. \(2015\)](#) documented the importance of local moisture sources associated with intense systems in the North Atlantic. Whether remote or

---

*Corresponding author address:* Bryan D. Mundhenk, Department of Atmospheric Science, Colorado State University, 1371 Campus Delivery, Fort Collins, CO 80523-1371.  
E-mail: [bryan.mundhenk@colostate.edu](mailto:bryan.mundhenk@colostate.edu)

local moisture sources dominate, ARs often contribute substantially to the water vapor flux within the atmospheric branch of the hydrologic cycle.

The majority of the recent work regarding ARs in the Pacific region focuses on these filamentary features making landfall along the west coast of North America, if not more specifically, along the contiguous U.S. West Coast. Furthermore, many of these recent studies are limited in scope to some manifestation of a Northern Hemisphere cool season or extended boreal winter (e.g., [Payne and Magnusdottir 2014](#); [Warner et al. 2015](#); [Kim and Alexander 2015](#)), perhaps due in part to their comparatively small study domains. Here we take a broader perspective and examine the climatology and large-scale variability of ARs in the North Pacific basin without restricting ourselves to landfalling and/or wintertime features. We aim to provide insight into the existence of ARs throughout the year, with a deliberate look at how their frequency of occurrence varies by location, by season, and by changes in the background state due to climate variability. In doing so, we will spatially and temporally expand upon the work of [Neiman et al. \(2008\)](#) who compared and contrasted a sample of summertime and wintertime ARs along the west coast of North America and noted seasonal differences in their character and impacts, but stopped short of assessing impacts due to variability beyond seasonality.

Earlier works by [Higgins et al. \(2000\)](#) and others revealed that tropical variability can influence the intensity and location of circulation anomalies in the extratropical Pacific and downstream, translating into variability in the poleward transport of water vapor. In specific reference to ARs, [Bao et al. \(2006\)](#) hypothesized the possible impacts that El Niño–Southern Oscillation (ENSO) may have on the direct transport of tropical moisture over the eastern Pacific, suggesting that such moisture exports are likely enhanced during ENSO neutral conditions and suppressed during El Niño periods. Similarly, [Ryoo et al. \(2013\)](#) detailed how ENSO may modify the subtropical jet and Rossby wave breaking near the U.S. West Coast, thereby impacting the region's tropospheric moisture transport and extreme precipitation events. Based on a detailed review of one winter's snow in California's Sierra Nevada, [Guan et al. \(2013\)](#) documented the potential impacts of large-scale variability (i.e., Arctic Oscillation, Pacific–North American teleconnection, and ENSO) on post-landfall AR-related impacts. Furthermore, [Payne and Magnusdottir \(2014\)](#) found that El Niño conditions result in an increase in the number of wintertime ARs making landfall along the west coast of North America and an equatorward shift in the mean latitude of landfall, while La Niña conditions reduce the number of

wintertime landfalling ARs and shift the mean latitude of landfall poleward. Others have identified relationships between the Madden–Julian oscillation (MJO) and individual AR events over the Pacific Ocean ([Ralph et al. 2011](#)) and/or AR-related impacts following landfall along the U.S. West Coast ([Guan et al. 2012](#)).

The purpose of this study is to explore the climatology of ARs over the North Pacific and the impacts of seasonality and climate variability on AR frequencies within this domain. We first develop an alternative anomaly-based method to identify ARs from gridded data. We then evaluate the climatology of ARs over the North Pacific. Finally, we use a compositing approach to assess variability about this climatology due to 1) seasonality, 2) ENSO, 3) MJO, and 4) their interactions. To emphasize how these forms of variability impact local AR frequencies, we also examine AR incidence for five subregions within the broader North Pacific domain.

The remainder of this paper is organized as follows: data and methods are outlined in [section 2](#), the climatology and variability of ARs in the North Pacific are presented in [section 3](#), further discussion and the conclusions of this study are found in [section 4](#), and an [appendix](#) provides additional information regarding the AR detection algorithm.

## 2. Data and methods

### a. Data sources

#### 1) ATMOSPHERIC VARIABLES

We employ the National Aeronautics and Space Administration's Modern-Era Retrospective Analysis for Research and Applications (MERRA) reanalysis dataset as the source for all atmospheric variables in this study. Even though the MERRA dataset was chosen because of its refined representation of the atmosphere's hydrological cycle ([Rienecker et al. 2011](#)), other studies have found few differences among the suite of current generation reanalyses in their representation of ARs (e.g., [Lavers et al. 2012, 2013](#)). A total of 36 years (1979–2014) of instantaneous horizontal winds and specific humidity were retrieved at native spatial resolution ( $1/2^\circ$  latitude  $\times$   $2/3^\circ$  longitude) and 6-h temporal resolution on isobaric surfaces. The use of instantaneous fields is preferential for the objective detection of AR-like filamentary features; additionally, the subdaily temporal resolution is favored for the study of features that may exist at or near their maximum intensity for less than one day.

#### 2) EL NIÑO–SOUTHERN OSCILLATION

ENSO conditions are characterized by the oceanic Niño index (ONI), the National Oceanic and Atmospheric

Administration's (NOAA's) official ENSO indicator, which is based on a 3-month running mean of sea surface temperature anomalies in the east-central tropical Pacific Ocean. Following NOAA's conventions, ENSO warm and cold events (El Niño and La Niña, respectively) are defined by ONI values meeting or exceeding threshold values of  $0.5^{\circ}$  and  $-0.5^{\circ}\text{C}$ , respectively, for a minimum of five consecutive overlapping seasons. In this work, ENSO neutral conditions are defined as all seasons wherein the ONI value falls between  $-0.5^{\circ}$  and  $0.5^{\circ}\text{C}$ ; however, defining ENSO neutral conditions by ONI values between  $-0.3^{\circ}$  and  $0.3^{\circ}\text{C}$ , in order to provide greater separation between the phases, has little impact on the results. These conventions applied to the ONI based on the Extended Reconstructed SST (ERSST) version 3b dataset (see [Smith et al. 2008](#)) results in 98, 108, and 201 overlapping 3-month periods defined as El Niño, La Niña, and neutral, respectively. Additionally, the El Niño composites described in [section 3](#) include all qualifying periods, regardless of whether the period was more reflective of an eastern Pacific or a central Pacific (also known as Modoki) warm event (see [Capotondi et al. 2015](#)). Combining eastern and central Pacific warm events may subdue the possible ENSO-related signals in the El Niño composites; however, composites based on the El Niño subtypes are noisier than the combined composite due to the smaller number of periods in each composite.

### 3) MADDEN–JULIAN OSCILLATION

The strength and evolution of the MJO is indicated by the real-time multivariate MJO index (RMM), as developed by [Wheeler and Hendon \(2004\)](#). In this work, unless specified otherwise, an MJO event is retained in a phase composite analysis if the RMM indicates the same phase for at least four consecutive days and the amplitude of the index meets or exceeds 1.5 standard deviations (sigma) at least once during the phase event. The 1.5-sigma threshold was selected to focus the analysis on only the strongest MJO phase events; however, reducing the threshold to 1 sigma has little impact on the conclusions.

#### *b. ARs defined*

##### 1) CALCULATION OF IVT

As discussed by other authors (e.g., [Lavers et al. 2012](#); [Gimeno et al. 2014](#)), two different spatial fields are commonly used to detect ARs: some form of precipitable water and some form of integrated water vapor transport (IVT). In this work we define ARs in terms of IVT, also referred to as vertically integrated moisture flux. We follow [Lavers et al. \(2012\)](#) and others and calculate the magnitude of IVT as

$$\text{IVT} = \sqrt{\left(\frac{1}{g} \int_{1000}^{300} qu \, dp\right)^2 + \left(\frac{1}{g} \int_{1000}^{300} qv \, dp\right)^2},$$

where  $g$  is gravitational acceleration,  $q$  is specific humidity,  $u$  is zonal wind,  $v$  is meridional wind, and  $dp$  is the pressure difference between adjacent pressure levels. The mass-weighted vertical integration is performed using data from 1000 to 300 hPa; however, the value of IVT is insensitive to the upper bound of the integral given the generally modest water vapor content of the upper troposphere.

The mean and first two harmonics of the IVT time series are removed at each grid point via fast Fourier transform in order to exclude the seasonal cycle and to create anomaly fields in which to detect AR-like features. The use of such anomalies removes the slowly varying features, such as the semi-persistent tropical moisture reservoir, thus much of the potential for low-latitude AR “false positives” that may plague methods using full values of IVT. The use of anomalies also facilitates the use of a static  $250 \text{ kg m}^{-1} \text{ s}^{-1}$  anomalous IVT threshold within the detection algorithm that does not itself vary seasonally, but that actually varies spatially and temporally across the domain in terms of an equivalent full IVT detection threshold (see [Fig. A1](#) in the [appendix](#)). Adjusting the number of harmonics removed within reasonable bounds has little impact on the resulting instantaneous anomaly fields or the performance of the detection algorithm.

##### 2) IDENTIFICATION OF ARs

The AR-like features, hereafter simply referred to loosely as ARs, are objectively identified within the fields of anomalous IVT via the automated detection algorithm described in the [appendix](#). We are certainly not the first to apply a detection algorithm to a reanalysis dataset to quantify ARs, but are motivated to do so in order to further investigate AR dynamics and variability. We aim to explore ARs over the entire North Pacific and throughout the entire year, thus requiring a more generalized methodology compared to many previously developed algorithms. This algorithm takes an occurrence-based approach (i.e., one AR hit for each time step during which the requisite intensity and geometric criteria are met); therefore, each time step is scrutinized independently. As a result, the AR frequencies described in this work are calculated based on the number of periods during which an AR exists over a given grid point divided by the number of periods included in the composite (see the [appendix](#) for additional details). Similarly, the numbers of AR periods listed herein represent the total number of 6-h periods during which

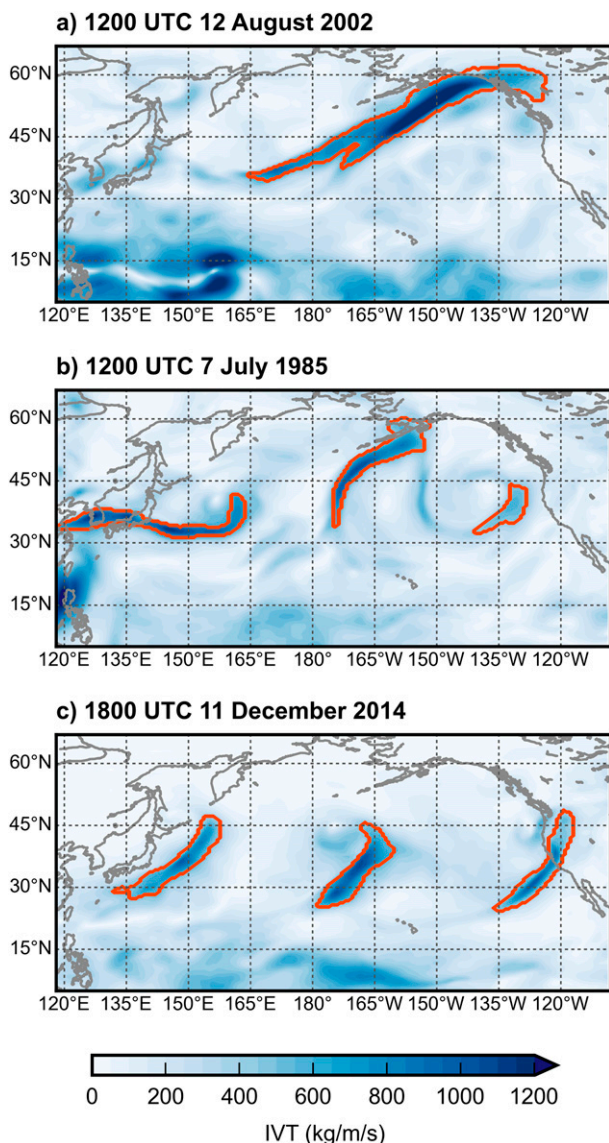


FIG. 1. Examples of detected AR-like features (outlined in red) within fields of instantaneous full-field IVT (shaded,  $\text{kg m}^{-1} \text{s}^{-1}$ ) for (a) 1200 UTC 12 Aug 2002, (b) 1200 UTC 7 Jul 1985, and (c) 1800 UTC 11 Dec 2014.

ARs were detected, not counts of independent AR events. Figure 1 depicts three example time steps during which ARs are identified by the algorithm, with the outlines of the detected features superimposed on fields of full IVT. Figure 1a shows an expansive summertime AR making landfall over the Alaska Panhandle, Fig. 1b displays three less traditional ARs, and Fig. 1c reveals a series of ARs that impacted the west coast of North America in December 2014. As described in the appendix, running the detection algorithm over the entire 36-yr period at 6-h resolution results in 81 409 retained features identified as ARs that have a center of mass

within the North Pacific domain ( $10^{\circ}$ – $64^{\circ}\text{N}$ ,  $123^{\circ}\text{E}$ – $118^{\circ}\text{W}$ ), as defined by the map area of Fig. 2. The total of 81 409 AR features equates to an average of approximately 1.5 features per 6-h time step. Again, the total number of AR features is a summation of occurrences detected within the 6-h time steps and should not be construed as analogous to independent AR events.

### 3. Results

#### a. Climatology

The output from the detection algorithm affords a calculation of, among other things, an all-season climatology of AR frequency within the North Pacific domain, as displayed in Fig. 2. The contouring in Fig. 2 reveals a maximum frequency of just over 13% near  $33^{\circ}\text{N}$ ,  $168^{\circ}\text{E}$  and frequencies in excess of 1% throughout the basin poleward of approximately  $20^{\circ}\text{N}$ . Interestingly, ARs identified via this methodology are found to be at least as frequent in places such as along the Aleutian Islands and near mainland Japan as they are along the U.S. West Coast. The frequency gradient that extends across the basin bracketing the Tropic of Cancer is robust to the method and appears to be tied to Rossby wave dynamics and the climatological northern extent of the Hadley circulation (not shown). The climatological depiction in Fig. 2 resembles the North Pacific portion of the 2-yr global climatology of ARs in Waliser et al. (2012). Differences between this climatology and those based on tropical moisture exports (e.g., Knippertz et al. 2013) may be due to our inclusion of AR-like features sustained by local moisture flux convergence and evaporation processes not exclusively tied to the transport of moisture from the tropics into the midlatitudes. Although the actual frequency values plotted in Fig. 2 are sensitive to the static thresholds within the detection algorithm, the spatial relationships are robust. This climatology provides useful reference values against which we will assess the impacts of seasonal and tropical variability on AR frequencies.

#### b. Seasonal variability

The first class of variability we will explore is the seasonal cycle. As noted above, the majority of recently published work related to ARs in the North Pacific focused on some representation of an extended boreal winter season. Those same studies often concentrated only on ARs making landfall along the U.S. West Coast or some subdivision thereof. As shown in Fig. 3, such a wintertime focus on landfalling features neglects sustained or even enhanced activity over the North Pacific during other seasons. The cyan curve represents the



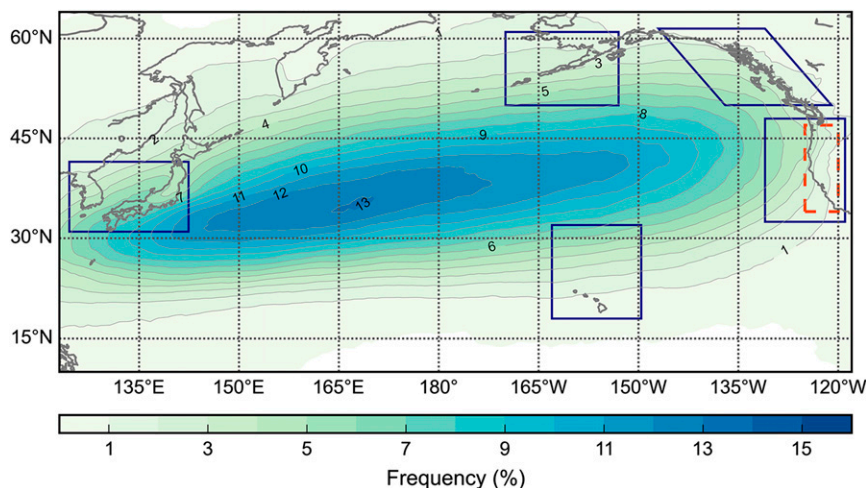


FIG. 2. All-season mean frequencies of AR occurrence over the North Pacific. The five blue-outlined boxes denote the locations that are used for in-depth, subregional analyses; the region identified by the dashed orange boundary is used to approximate U.S. West Coast landfalling events for Fig. 3.

mean number of AR periods detected near the U.S. West Coast during overlapping 3-month seasons, scaled to represent uniform 90-day seasons. The ARs near the U.S. West Coast exhibit a pronounced seasonal cycle, with a minimum during boreal summer and a maximum during boreal winter. However, the gray curve representing the mean number of AR periods detected within the entire North Pacific domain does not display that same seasonality, suggesting that the seasonality of ARs varies by location within the domain. Moreover, the substantial separation between the curves in Fig. 3

reveals the small proportion of ARs occurring near the U.S. West Coast compared to the basinwide total. At times considered to be only rare or extreme events, analyses such as this emphasize that ARs are nearly ever-present contributors to the hydrological cycle on a basinwide scale.

While statements that ARs making landfall along the U.S. West Coast are most common during the boreal winter are supported by this analysis, the seasonality of AR frequencies varies strongly by region. To illustrate this point, Fig. 4 displays the mean number of AR

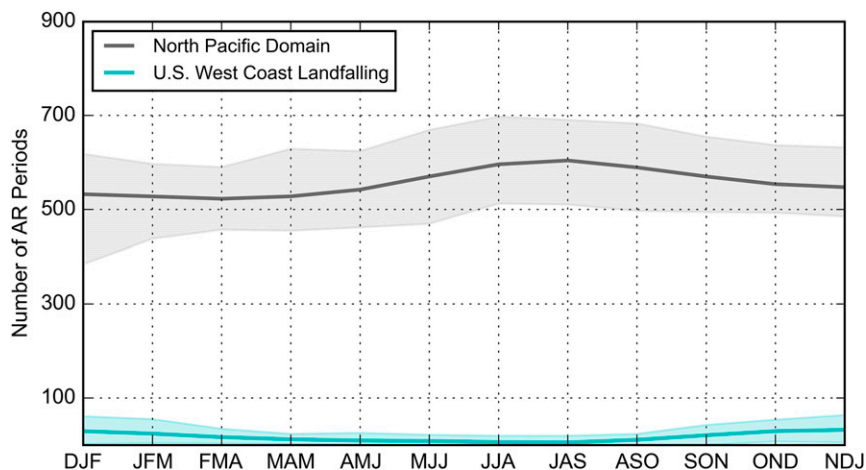


FIG. 3. Comparison between the mean number of AR periods within the entire North Pacific domain ( $10^{\circ}$ – $64^{\circ}$ N,  $123^{\circ}$ E– $118^{\circ}$ W) and within a subregion that encompasses much of the U.S. West Coast (identified by the dashed orange outline in Fig. 2) by overlapping 3-month seasons. The lines represent the seasonal mean over the 36-yr record, while the shading highlights the range between the highest and lowest seasonal values. All seasons are scaled to represent uniform 90-day seasons.

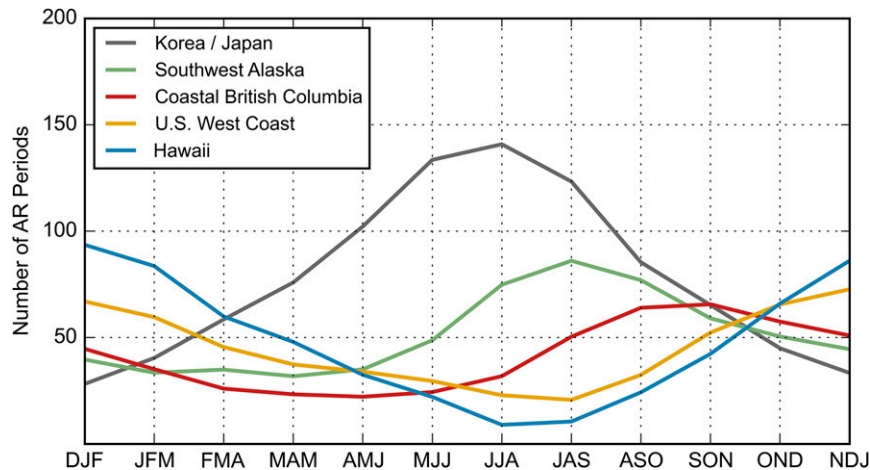


FIG. 4. As in Fig. 3, but of the mean number of AR periods for the subregions described in the text and depicted in Fig. 2. Shading is omitted for clarity.

periods by overlapping 3-month seasons for the five subregions outlined in Fig. 2. These locations are not studied for their distinct depiction of AR variability per se, but rather for their potential societal importance. Regardless, differences among the locations' AR seasonal cycles are apparent in Fig. 4. For example, the Korea–Japan subregion (gray curve), with a clear peak in AR occurrence in June–August (JJA), displays a seasonality nearly opposite to that of the U.S. West Coast. Additionally, a comparison of the southwestern Alaska, coastal British Columbia, and U.S. West Coast mean numbers of AR periods (green, red, and amber curve, respectively) shows that the seasonal maximum AR occurrence shifts earlier in the year—toward the warm seasons—with an increase in latitude along the North American coast, similar to the behavior observed by Neiman et al. (2008).

Taking a spatial, basinwide perspective, Fig. 5 reveals remarkable location-dependent changes in AR frequency with season, here represented as the difference between JJA or December–February (DJF) AR frequency and the all-season mean AR frequency. The nearly opposing patterns in the two panels of Fig. 5 are more indicative of a spatial shift in AR incidence, rather than an overall seasonal increase or decrease in basinwide AR occurrence. The depicted patterns of frequency difference are consistent with the previously observed wintertime peak in AR frequencies along the U.S. West Coast and the seasonal contrast in that region suggested by Figs. 3 and 4. The contrasting panels also capture the warm-season increase in AR activity near Alaska mentioned earlier, out of phase with the seasonality observed near California and the Pacific Northwest. Seasonal differences in the range of 1%–8% are not

trivial considering that the maximum all-season AR frequency of occurrence is only approximately 13% in the heart of the domain, with most locations having a considerably lower mean AR frequency.

Figures 4 and 5 also begin to reveal the complexity of AR behavior near eastern Asia relative to other parts of the North Pacific domain, behavior previously documented by Knippertz and Wernli (2010) in terms of tropical moisture exports. The pronounced summertime peak in AR numbers in the Korea–Japan subregion in Fig. 4 (gray curve) and the comparatively large positive values of frequency difference near the Korea Peninsula and Japan in Fig. 5a relate to increased summertime activity in that region associated with the East Asian monsoon. A visual review of a subset of the detected summertime ARs in that region indicates an interesting mix of features, some not unlike the ARs detected elsewhere in the domain, while others appear as enhanced activity along the monsoonal mei-yu, baiu, and/or changma boundaries (see Sampe and Xie 2010, and references therein). The detection algorithm does filter out conventional tropical cyclones, but may retain AR-like features associated with transitioning–recurring tropical cyclones (e.g., Cordeira et al. 2013), tropical synoptic systems (e.g., Maloney and Dickinson 2003), and elongated regions of enhanced IVT along the semi-persistent monsoon boundaries. The far western Pacific–eastern Asia region is included in this work because of its importance in the life cycle of the systems that support ARs elsewhere in the domain, and for societal reasons.

The latitudinal shift in frequencies apparent in Fig. 5 may be associated with the well-documented seasonal migration of eddy activity along the eddy-driven jet (see Riehl et al. 1950, and others). Figure 6 compares the

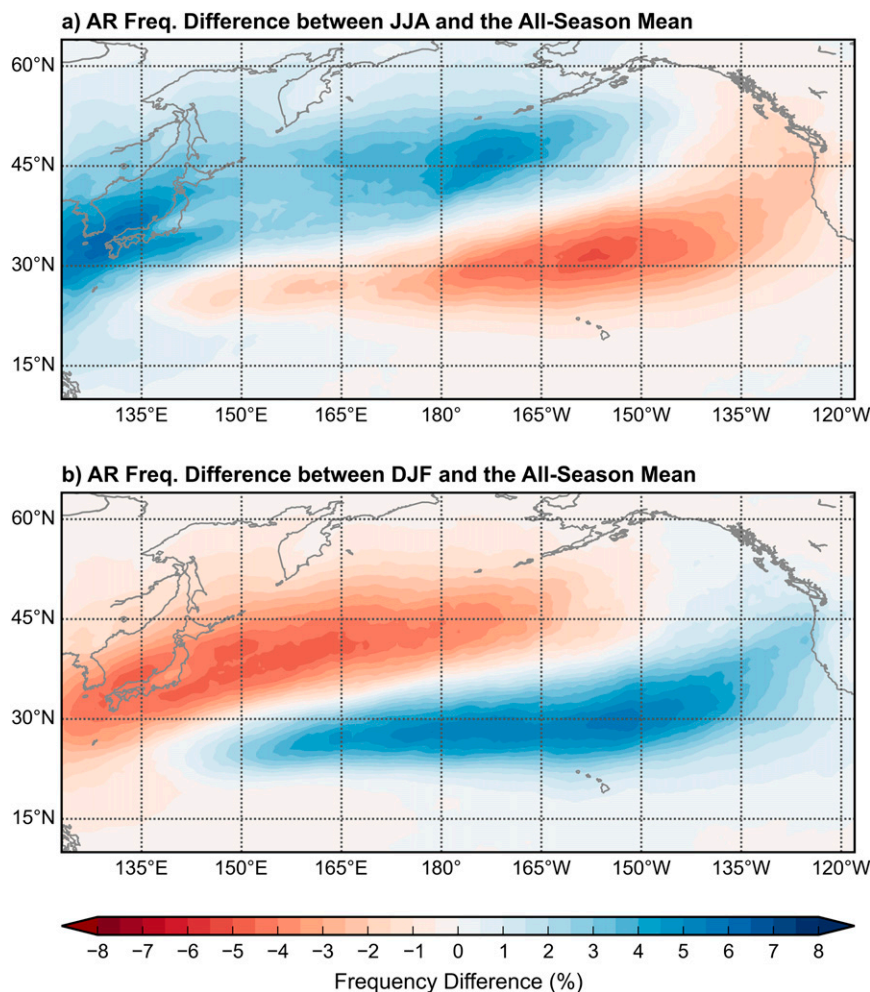


FIG. 5. The AR frequency differences for (a) JJA and (b) DJF resulting from the subtraction of the all-season AR frequencies for the period 1979–2014 from the seasonal composite frequencies. Positive (blue) [negative (red)] values indicate seasonal frequencies of occurrence higher (lower) than the annual mean.

seasonal latitudinal migration of the eddy-driven jet with the mean position of maximum AR frequencies across the domain. Here, we follow standard practice and calculate the jet latitude by computing the latitude of the maximum low-level zonal mean zonal wind, vertically averaged from 925 to 700 hPa, within the North Pacific domain (e.g., Woollings et al. 2010). Similarly, the position of the maximum AR frequency is computed based on the latitudinal position of the maximum zonal mean AR frequency. In Fig. 6, both the eddy-driven jet—used here as a proxy for eddy activity—and the AR frequency maximum are most poleward during boreal summer and most equatorward during boreal winter, suggesting a relationship between the position of the eddy-driven jet and AR activity in the North Pacific. Furthermore, the equatorward offset of maximum AR

frequency compared to the jet position may be a result of Rossby wave breaking on the flank of the jet. As depicted in Fig. 10g of Barnes and Polvani (2013), Rossby wave breaking preferentially occurs approximately  $10^\circ$  equatorward of the jet throughout the year. Here we find that the frequency maximum of ARs also preferentially occurs  $10^\circ$  equatorward of the seasonal mean eddy-driven jet position. The relationship between Rossby wave breaking and ARs is an area of ongoing research (e.g., Ryoo et al. 2013; Sodemann and Stohl 2013; Payne and Magnusdottir 2014), but ventures beyond the scope of this work.

### c. Tropical variability

The seasonal spread of the number of AR periods—indicated by the shaded regions in Figs. 3 and 6—suggests



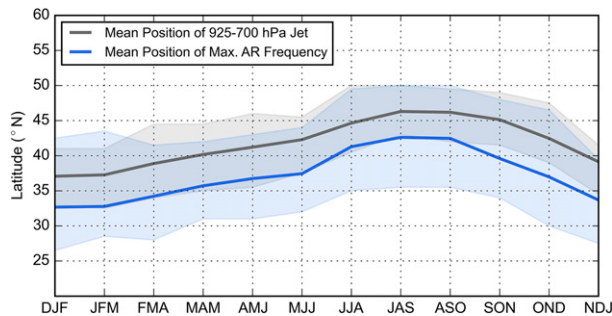


FIG. 6. Comparison of the latitudinal variation of the position of the eddy-driven jet stream (gray) and the position of the zonal mean maximum AR frequency (blue) by overlapping 3-month seasons within the North Pacific domain. The shading highlights the range between the highest and lowest seasonal values for each variable.

a fair amount of variability, a significant portion of which may be influenced by tropical variability. While the background atmospheric conditions in the North Pacific may be more conducive to support tropical teleconnections during boreal winter (e.g., Horel and Wallace 1981), we evaluate possible connections between tropical variability and AR activity during all seasons. Although other well-documented modes of tropical variability exist, we focus our assessment here on the leading modes of interannual and intraseasonal variability, ENSO and the MJO, respectively.

### 1) EL NIÑO–SOUTHERN OSCILLATION

Figure 7 shows frequency differences between ENSO phase composites and the all-season mean. The El Niño composite (Fig. 7a) depicts the impacts of an enhanced and extended jet (e.g., Arkin 1982) on AR activity, with statistically significant (at 90% confidence level based on 1000 bootstrap samples) positive anomalies along 30°N in the eastern Pacific and negative anomalies to the north along 45°N. In contrast, the enhanced activity extending from the central Pacific into the Gulf of Alaska in the La Niña composite (Fig. 7b) is reminiscent of the previously observed poleward displacement of the storm track. This pattern suggests that the displaced storm track shifts the extratropical cyclone activity, resulting in an overall poleward shift in AR occurrence. The ENSO neutral composite (Fig. 7c) is reminiscent of the JJA seasonal AR frequency difference composite in Fig. 5a, likely influenced by the disproportionate number of ENSO neutral periods occurring during warm seasons and the fact that El Niño and La Niña events tend to peak in amplitude during the winter half-year.

Capturing the impacts of tropical variability on AR activity is complicated by the marked seasonality of ARs within the North Pacific domain shown earlier. Figure 8

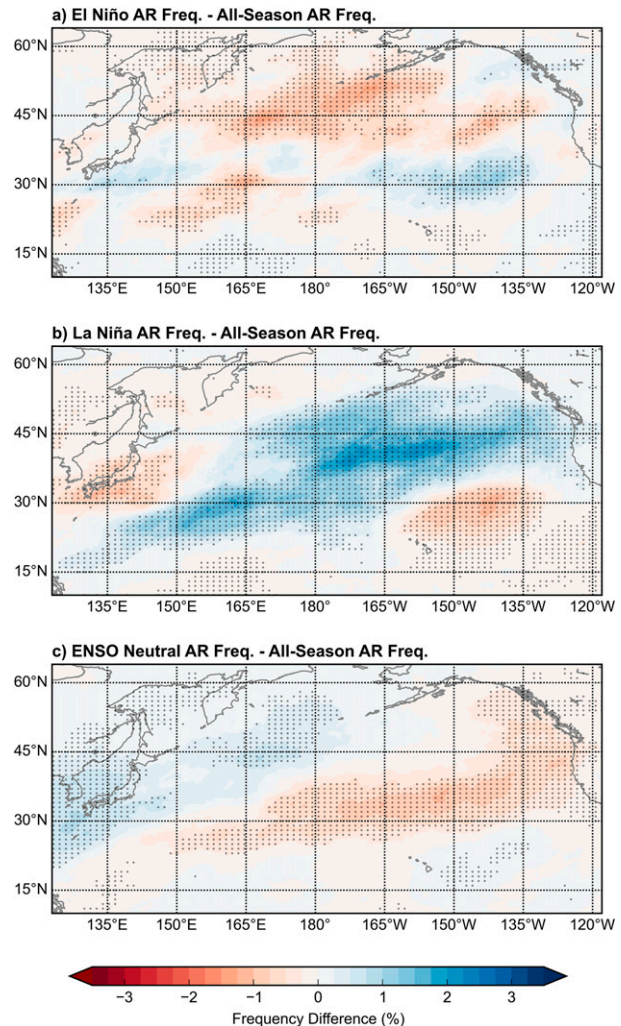


FIG. 7. As in Fig. 5, but comparing AR frequencies composited based on ONI values for (a) El Niño, (b) La Niña, and (c) ENSO neutral conditions with the annual mean AR frequencies removed. Stippled regions denote significance at the 90% confidence level based on 1000 bootstrap samples.

displays the frequency differences between ENSO composites and the respective seasonal mean AR frequencies for two opposing seasons: JJA (left column) and DJF (right column). As presented, Fig. 8 reveals that ENSO-related impacts vary by season. The classic El Niño and La Niña signals relating to the modification of the storm track and Rossby wave train response to ENSO-like heating (e.g., Hoerling and Kumar 2002) are most apparent in the enhanced AR frequency anomalies during the cool season (DJF). However, the large, statistically significant frequency differences during the warm season (JJA) suggest that ENSO may influence AR activity throughout the year. Also visible are the impacts of the seasonal cycle of AR frequencies on the



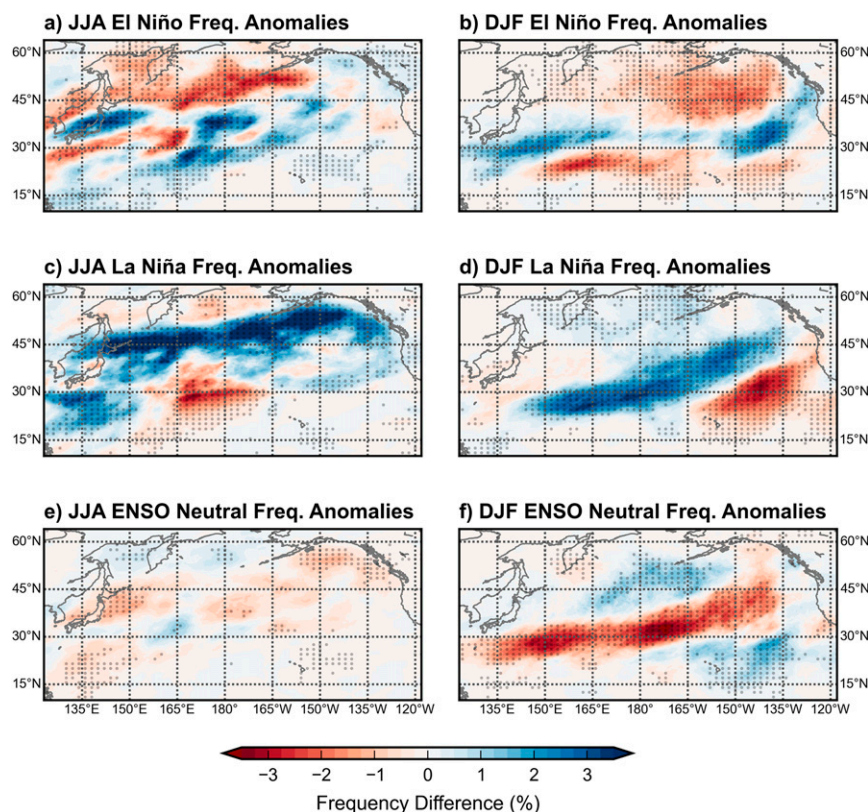


FIG. 8. As in Fig. 7, but comparing AR frequencies composited based on ONI values for (a),(b) El Niño; (c),(d) La Niña; and (e),(f) ENSO neutral conditions with the seasonal mean AR frequencies removed for (left) JJA and (right) DJF. Note that the range of values used for the color fill is equivalent to that used in Fig. 7, but different from the range displayed in Figs. 5 and 10. Stippled regions denote significance at the 90% confidence level based on 1000 bootstrap samples.

seasonal ENSO phase composites; for example, the poleward enhancement of ARs during DJF La Niña periods is displaced farther poleward during JJA La Niña periods, likely due to the seasonal shift in the AR activity shown in Fig. 6. Although the stippling indicates regions where the frequency differences are significant at the 90% confidence level, we confirmed that the majority of 3-month periods within each composite display frequency anomalies of the same sign and similar distribution as those depicted in each of the panels, supporting the robustness of these spatial patterns of ENSO-related impacts.

To further illustrate the impacts of ENSO and the seasonal cycle on AR occurrence, we return to the five subregions described earlier. Rather than presenting AR frequencies or frequency differences, we present the impacts of El Niño and La Niña on AR frequencies in Fig. 9 in terms of the percent change relative to the local, seasonal mean AR frequencies. Here statistical significance is based on a  $t$  test comparing the seasonally

composited El Niño and La Niña values, with the degrees of freedom being the number of seasonal El Niño and La Niña events combined minus two. This representation of ENSO's impact on AR frequencies, in terms of percent change, varies based on location and season. Although not highlighted as being statistically significant by the  $t$  test—likely due to the limited reanalysis record—AR frequencies along the U.S. West Coast are increased during El Niño events, but only during winter months when ARs are climatologically most common. In contrast, El Niño conditions may actually reduce AR activity during summer months along the U.S. West Coast. Another feature that emerges is that the greatest impacts relating to ENSO variability do not always occur during boreal winter; indeed, several locations show peak changes of approximately 40% during the warm seasons (e.g., near Hawaii and along the coast of British Columbia). Also, El Niño and La Niña do not always have opposing impacts on a location; for example, during much of the summer half-year in the

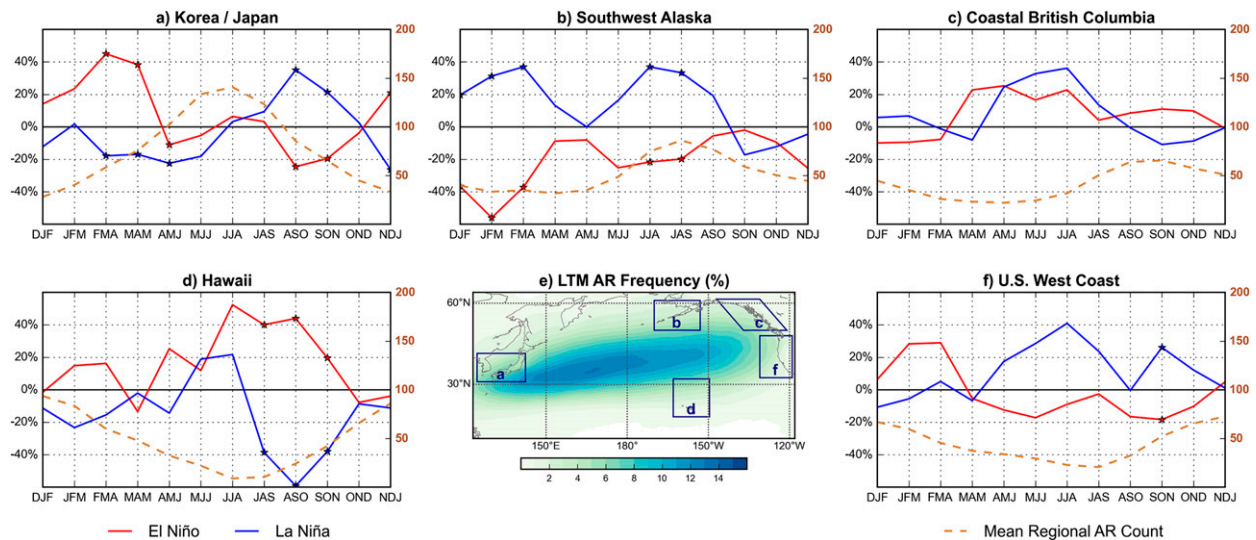


FIG. 9. Analyses of seasonal variability in terms of percent change in subregional AR frequency compared to the 3-month seasonal mean for the (a)–(d), (f) five locations identified in (e) (and in Fig. 2). For each location, lines representing El Niño (red) and La Niña (blue) conditions are plotted based on the legend and aligned with the vertical axis on the left-hand side of each panel. ENSO-neutral conditions are omitted for clarity. Also included in each panel is a depiction of the seasonality of the mean number of AR periods within the location's bounds according to the vertical axis on the right-hand side of each panel (dashed brown line). Stars in each panel indicate seasons where the percent change in AR frequency for El Niño periods is statistically significant from La Niña periods at the 90% confidence level based on a  $t$  test.

coastal British Columbia subregion both El Niño and La Niña conditions increase AR activity above the seasonal norm (Fig. 9c). Furthermore, in comparing ENSO's impacts on AR frequencies with the climatological seasonal cycle of the number of AR periods (e.g., the dashed brown lines in Fig. 9), it emerges that ENSO variability can greatly alter the seasonal cycle. For example, the southwestern Alaska subregion (Fig. 9b) sees an average of approximately 40 AR periods during the scaled 90-day February–April (FMA) season. A local El Niño–related decrease of AR frequency of approximately 40% during that period could decrease that seasonal norm of 40 AR periods down to approximately 24 AR periods. In contrast, La Niña conditions stem a mean increase in AR activity, resulting in a mean of nearly 56 AR periods in that subregion during FMA.

## 2) MADDEN–JULIAN OSCILLATION

Transitioning from ENSO's interannual scale to MJO's intraseasonal scale, we present Fig. 10 with its eight RMM-based MJO phase composite AR frequencies, each with the all-season AR frequency removed. The panels in Fig. 10 depict a somewhat progressive evolution of patterns of positive and negative values of frequency difference anomalies during an MJO life cycle. Most pronounced are the higher frequencies of AR occurrence in the central and eastern Pacific during phases 7 and 8, when the anomalous convective activity

associated with the MJO is transitioning from the Pacific to the Western Hemisphere. The increased AR activity depicted in the eastern Pacific during phases 6–8 may be linked to an enhanced eddy-driven jet resulting from the anomalous convection, with impacts similar to the El Niño composites but on a different time scale.

Figure 11 revisits the five subregions to further assess the MJO impacts on AR frequencies. The composited MJO impacts on AR frequency anomalies vary by location. For example, AR frequencies are reduced near Hawaii when the anomalous heating associated with the MJO is in the Indian Ocean (phases 2 and 3) and over the Maritime Continent (phases 4 and 5), then frequencies are enhanced as the active convection progresses from the western Pacific into the Western Hemisphere (phases 6–8). In contrast, AR frequency anomalies in the subregion encompassing much of the Korea Peninsula and Japan show a nearly opposite and weaker response to that of the subregion surrounding Hawaii. Although not as pronounced as the AR frequency impacts near Hawaii, Fig. 11f indicates a reduction in ARs near the U.S. West Coast when the active phase of the MJO is near the Maritime Continent (phases 4 and 5) and an increase in ARs approaching the U.S. West Coast when the MJO is in phases 7 and 8. The panels displayed in Fig. 11 are based on the average subregional AR frequency impact during MJO phase



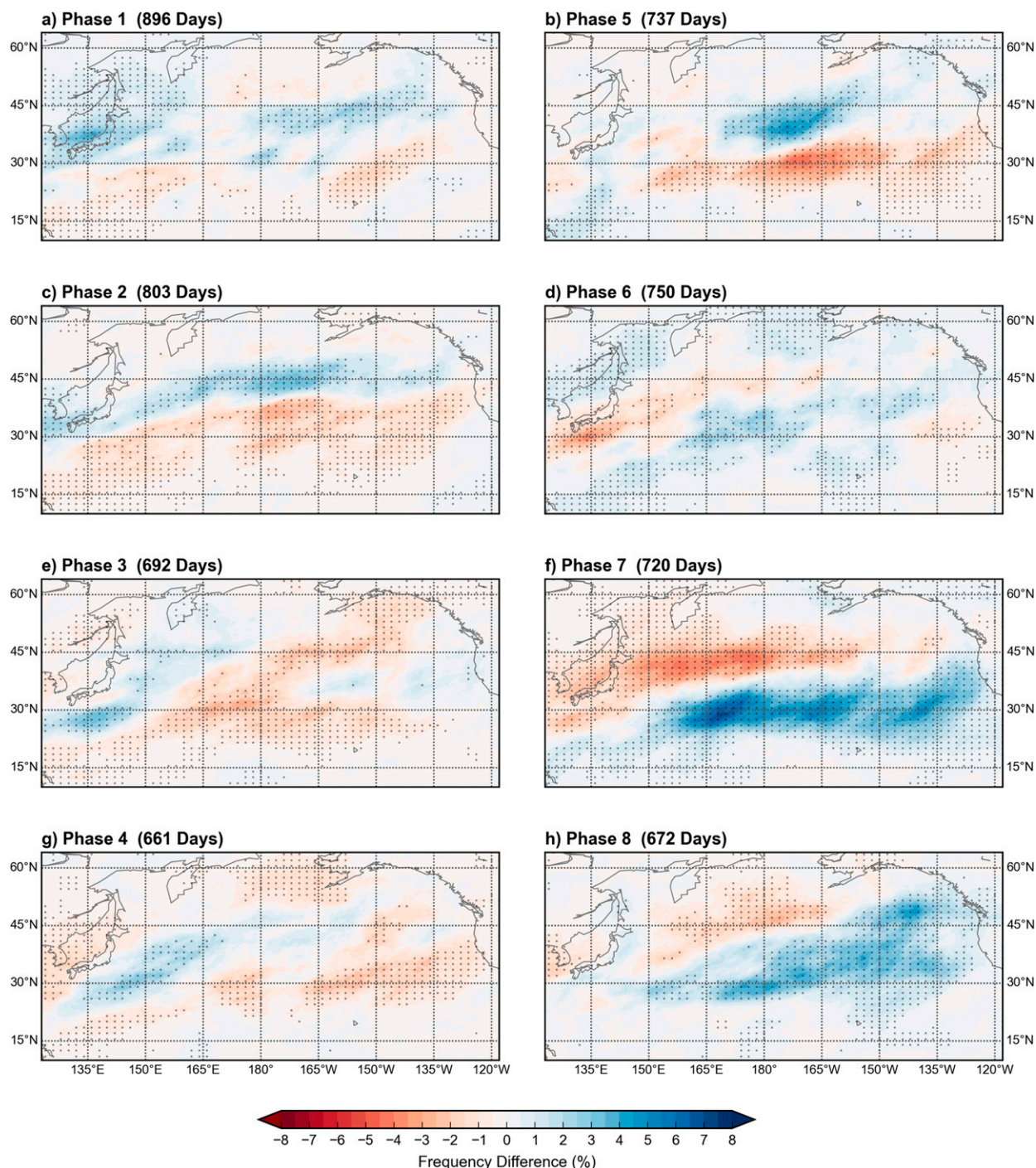


FIG. 10. As in Fig. 7, but for RMM-based MJO phase composites with the annual mean AR frequencies subtracted. As described in the text, only periods when the RMM index remained in the same phase for at least 4 consecutive days and during which at least 1 day had an RMM index amplitude  $\geq 1.5$  standard deviations are composited. Stippled regions denote significance at the 90% confidence level based on 1000 bootstrap samples.

events compared to mean AR frequencies. An alternate approach comparing the number of AR hits within each subregion—like that used for the earlier AR period count plots—provides similar results (not shown).

We have shown that most locations have a pronounced seasonal cycle in AR frequencies and that seasonality matters when considering ENSO's impact on AR incidence; therefore, it is natural to wonder

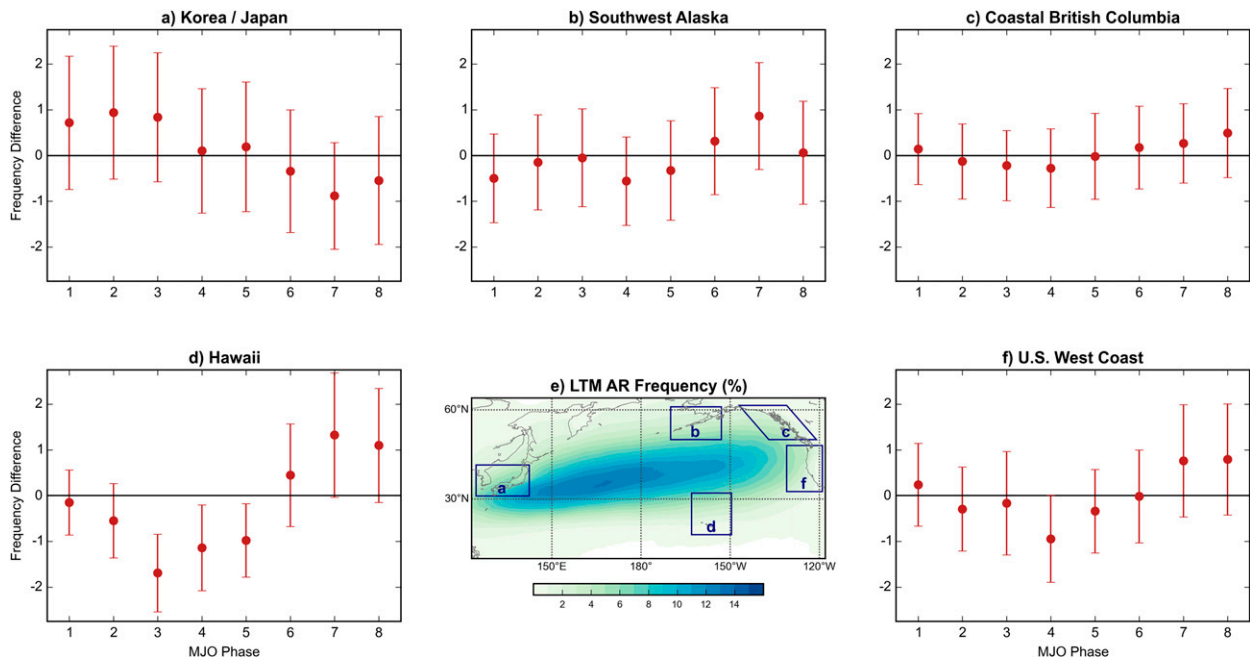


FIG. 11. MJO phase composite frequency anomalies by (a)–(d), (f) subregions as a function of MJO phase. Error bars encompass a 90% confidence interval based on the estimated standard error of sample proportions using the number of periods in each composited phase as the sample size.

whether these all-season MJO composites are being muted by seasonality. Figure 12 depicts the percent change in AR frequency (as in Fig. 9) in paired MJO phase composites compared to the seasonal mean AR frequencies for the five subregions. Here the phases are paired (1 and 2, 3 and 4, and so on) to reduce the noise and increase plot clarity. This subregional analysis reveals how an all-season assessment of MJO-related impacts will subdue, if not completely mask, the seasonal impacts within a region. For example, the Korea–Japan subregion in Fig. 11 displays a modest frequency response due to MJO forcing; however, Fig. 12 reveals that the MJO activity may result in significant frequency changes of 25%–50% during certain seasons (e.g., AR frequency increase in excess of 50% during DJF with MJO’s active convection captured by RMM phase 1 and 2). Indeed, all five subregions show paired phase frequency responses of at least 50% during one or more seasons. As with ENSO-related variability, Fig. 12 suggests that MJO-related variability has the potential to significantly counter or enhance low-frequency variability like the seasonal cycle or ENSO background with respect to AR frequencies, but on a shorter time scale.

These MJO relationships are evaluated without a lag or lead separating the MJO event and the AR impacts. Depending on the location within the domain and dynamical mechanisms making the teleconnection, MJO-related forcing takes time, on the order of days

to weeks (e.g., Hoskins and Karoly 1981; Matthews 2004; Branstator 2014), to evolve and communicate across the basin. However, the domainwide view of this work complicates the evaluation of lagged response to MJO-like heating in such a manner, as the MJO response presumably takes differing lengths of time to impact different locations in the domain. Quantifying the lag–lead relationships and identifying the dynamical aspects of MJO-like heating that are most impactful to downstream AR relationships will remain for future work.

### 3) VARIABILITY INTERACTIONS

The results presented here suggest that variability due to ENSO and the MJO can compound or negate each other and have profound impacts on the occurrence of ARs in the North Pacific. Figure 13 examines the five subregions once again, but in terms of AR frequency anomalies within each region binned by ONI values—representing the state of ENSO—and RMM-based MJO phases. The binned, composited AR frequency anomaly values are standardized to more clearly reveal those ENSO–MJO combinations that result in changes in AR occurrence and to allow for a visual intercomparison of the subregions. Each panel is generated based on 845 independent high-amplitude MJO phase occurrences, each binned according to the coincident state of ENSO. Bins containing fewer than 10 phase



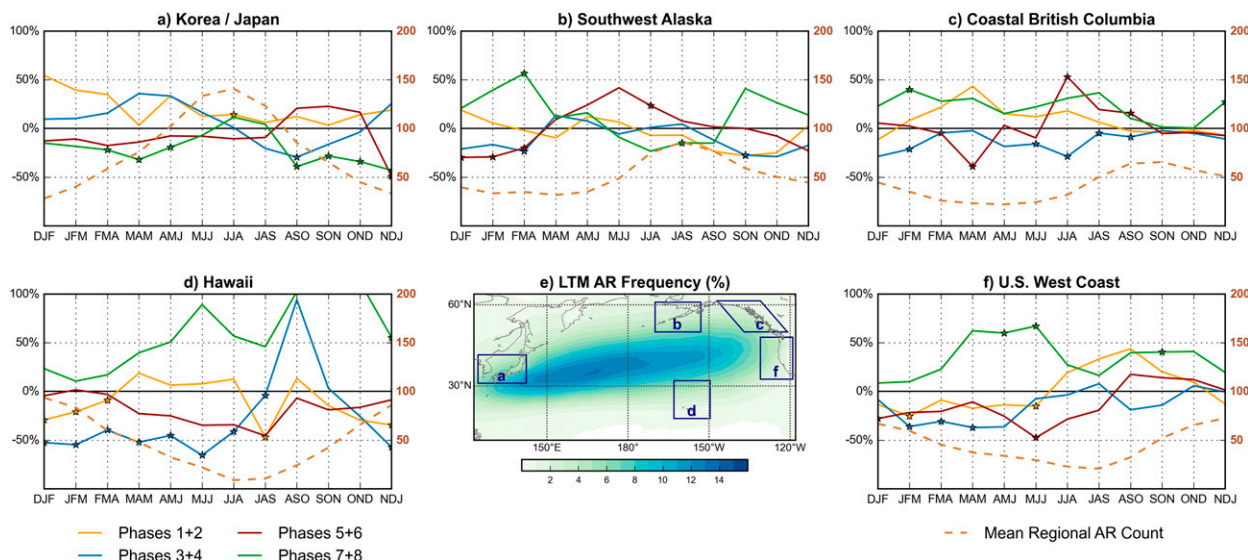


FIG. 12. As in Fig. 9, but for the percent change of paired seasonal MJO phase composite frequencies compared to 3-month seasonal mean AR frequencies. Stars in each panel indicate season–phase combinations where the percent change in AR frequency from the seasonal mean AR frequency is statistically significant at the 90% confidence level based on a  $t$  test.

occurrences are masked and hatched. Apparent from these two-dimensional histograms is that the combined ENSO–MJO relationships are complicated and vary based on location. For example, AR activity near Hawaii

appears more dominated by MJO variability (left-to-right contrast in Fig. 13d) than ENSO variability (top-to-bottom contrast) in this all-season analysis, with the frequency of ARs being enhanced when MJO-like

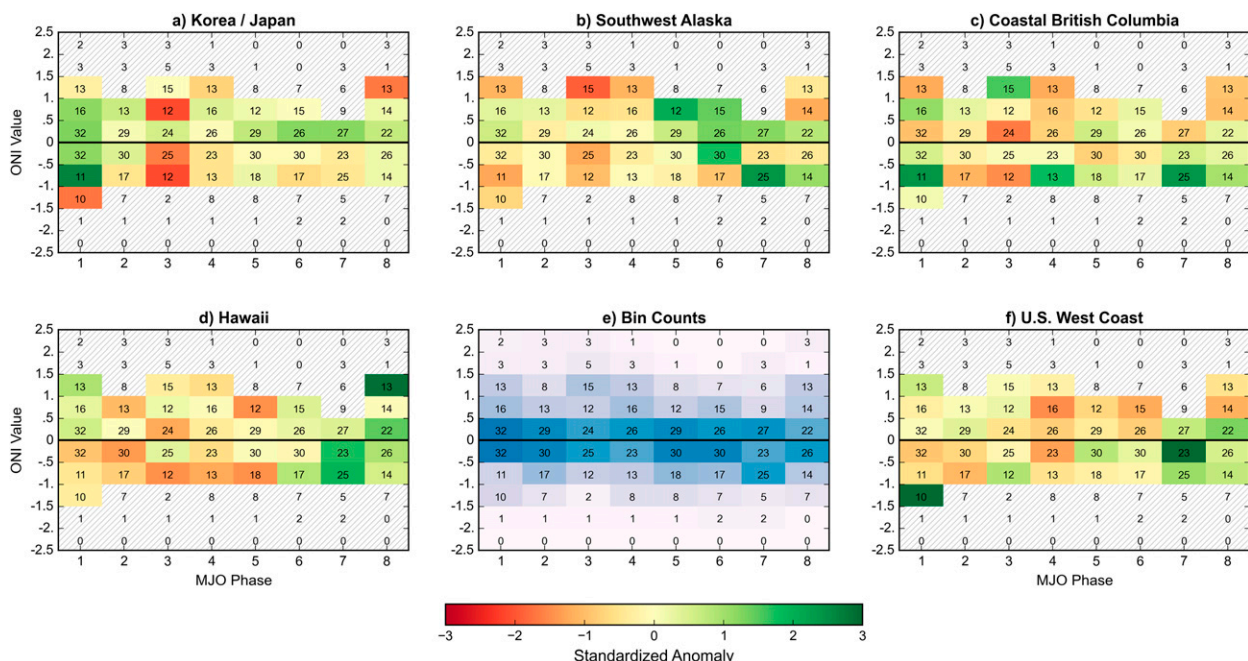


FIG. 13. Two-dimensional histograms of AR frequencies arranged by binned ONI values ( $^{\circ}\text{C}$ ) vs RMM-based MJO phase for (a)–(d), (f) the five subregions depicted in Fig. 2. (e) The number of independent MJO phase occurrence–ONI value pairs in each bin are shown and shaded and repeated as the numeric overlay in each of the panels. The AR frequency difference values are standardized for each region and represented by the bin color fill according to the color bar; bins with  $<10$  unique phase occurrences are masked and hatched.

heating is over the western Pacific and transitioning into the Western Hemisphere (phases 6–8). In contrast, the coastal British Columbia subregion generally shows enhanced AR activity (green shading) more preferentially during La Niña periods, while reduced AR activity (red shading) is more common during El Niño events. The complicated—perhaps even noisy—appearance of the panels in Fig. 13 is not unexpected, due to the anticipated complex interactions between modes of tropical variability. This may be especially true for these particular subregions—each chosen for their potential societal importance, not for their representation of AR variability—well removed from the high AR frequencies of the central North Pacific. Hence, more coherent anomaly patterns can be expected for subregions positioned over oceanic locations with more frequent AR activity.

#### 4. Discussion and conclusions

An automated detection algorithm is used to objectively identify ARs within 36 years of gridded reanalysis data. The resulting output allows for a compositing approach to investigate how the seasonal cycle and climate variability influence ARs over the North Pacific in the reanalysis record. Here we focus on the all-season climatology of ARs over the North Pacific, as well as the impacts of three forms of variability on AR frequencies of occurrence: seasonal cycle, ENSO, and MJO, as well as their interactions.

Atmospheric rivers exist throughout the year within the North Pacific domain, but a clear seasonality exists in the spatial distribution of AR frequency. This seasonal cycle of AR activity manifests itself more as a displacement of ARs toward the north and west during the warm seasons—in association with the seasonal migration of the eddy-driven jet—than it does in a marked change in the total number of ARs that occur within the North Pacific region.

Studies that focus only on some representation of the boreal winter season may provide incomplete assessments of ARs and their impacts across the Pacific. In particular, such focused work may miss important warm-season AR contributions to the general circulation and/or hydrologic cycle, especially for domains that extend beyond the U.S. West Coast. This issue may be particularly critical when investigating potential future changes in AR frequency and/or behavior, as examinations within limited temporal or spatial domains may mask shifts in the seasonal cycle or preferred locations of ARs. Additionally, statements regarding the seasonality of ARs must clearly specify the location(s) for which such statements apply, as the claims in current literature that more

ARs occur during the winter half-year (e.g., [Gimeno et al. 2014](#); [Payne and Magnusdottir 2014](#)) only hold true in specific subregions (such as near Hawaii and along the west coast of the contiguous United States).

Furthermore, the composite analyses undertaken here suggest a complex interaction between classes of variability and their impact on ARs. Changes to the seasonally varying North Pacific mean state due to the leading forms of interannual and intraseasonal tropical variability can enhance or offset the pronounced seasonal cycle and/or each other by forcing local changes upward of  $\pm 40\%$ – $50\%$  of the seasonal mean AR frequency of occurrence. As ENSO and the MJO can both modify the eddy-driven jet position and strength over the North Pacific, both are shown to impact the displacement and occurrence of ARs in a way not unlike the seasonal cycle, but on different time scales. This exploration into the large-scale variability of ARs in the North Pacific is not all-inclusive; indeed, one could imagine composites based on other characterizations of variability (e.g., Arctic Oscillation and Pacific–North American teleconnection) beyond those presented here.

Recently published work by [Guan and Waliser \(2015\)](#) largely corroborates the results of this investigation. They developed and documented an AR detection algorithm based on full-field IVT calculated from the ECMWF interim reanalysis (ERA-Interim) and using an 85th percentile detection threshold specific to each season and grid cell. Their depictions of global AR climatology and variability are similar to the North Pacific plots shown herein, especially after adjusting for differences in the period of record (18 vs the 36 yr used in this work), composite periods, and color bar conventions (not shown). This comparison lends credence to the robustness of both works' conclusions, despite the differences in detection methods and underlying datasets.

As ARs bridge weather and climate scales, this work addresses the climatology and variability in terms of actual AR occurrences versus a more general approach of investigating total or filtered fields of water vapor transport employed by others (e.g., [Newman et al. 2012](#); [Kim and Alexander 2015](#)). We postulate that our identified relationships between climate variability and water vapor transport would be similar even if some moisture flux variable or field was composited; however, this feature-based approach affords a more detailed observational examination and impact assessment of these weather-makers not afforded by a filtering or field approach.

Whether the likelihood of AR occurrence is altered by seasonality or tropical variability, AR impacts on day-to-day weather and seasonal climate anomalies are where these features matter most to forecasters,

resource managers, and the regional population. As shown, location and the state of the climate system matter when considering frequencies of AR occurrence and their potential impacts. As a result, the well-posed arguments made regarding the importance of considering wintertime landfalling ARs along the U.S. West Coast (heightened flood risk, hydrological budgeting, etc.) in earlier works (e.g., Ralph et al. 2006; Dettinger et al. 2011; Warner et al. 2012; Dettinger 2013) may also be applied to other subregions of interest, although the season and climate background state require consideration.

**Acknowledgments.** Thanks to NASA's Global Modeling and Assimilation Office and the Goddard Earth Sciences Data and Information Services Center for the hosting and dissemination of the MERRA reanalysis data used in this study. Thanks also to the three anonymous reviewers whose constructive comments and suggestions improved this manuscript. EAB and EDM are supported, in part, by the Climate and Large-Scale Dynamics Program of the National Science Foundation under Grants AGS-1419818 and AGS-1441916, respectively.

## APPENDIX

### Automated AR Detection Algorithm

#### a. Overview

This appendix outlines the atmospheric river (AR) detection algorithm that is used throughout this work. (The algorithm, written in the Python 2.7 programming language, is available online at <http://hdl.handle.net/10217/170619>.) This algorithm follows the objective detection approaches of others (e.g., Lavers and Villarini 2013; Wick et al. 2013; Payne and Magnusdottir 2014), but employs a unique technique of detecting AR-like features from within fields of anomalous integrated water vapor transport (IVT). The use of anomalies was found to be efficient and to benefit automated feature detection in large spatial (i.e., North Pacific) and temporal (i.e., sub-daily across all seasons) domains. Additionally, this algorithm was developed to facilitate climatological and dynamical analyses and compositing, more so than to output a definitive AR event atlas.

As in Nayak et al. (2014), no temporal persistence is required for the identification of an AR by this algorithm. In this approach, each feature of interest and time step is scrutinized independently. Differences, perhaps subtle, should be expected in output from an algorithm tuned to detect an event (i.e., one hit per feature life cycle) versus this occurrence-based (i.e., one hit for each time step during which the criteria are met) approach. The AR

frequencies of occurrence in this research are calculated based on the number of periods during which a detected AR exists over each grid point divided by the number of periods in the composite. Additionally, the presented AR period counts are determined by the number of periods during which an AR-like feature extended sufficiently into the subregion of interest, not as a count of distinct ARs per se. While such results may be weighted by persistent events, this influence is not inappropriate as the persistence of an AR over an area greatly affects its potential impacts (Ralph et al. 2013).

#### b. Methodology

The algorithm begins by reading in precalculated IVT data. Scrutinizing each 6-h period separately, a two-dimensional array of IVT anomaly values is created by removing the IVT mean and seasonal cycle as described in section 2. An anomalous IVT magnitude threshold of  $250 \text{ kg m}^{-1} \text{ s}^{-1}$  is then used to isolate so-called features of interest. While the  $250 \text{ kg m}^{-1} \text{ s}^{-1}$  anomaly threshold is itself static and fixed within the algorithm, the comparable full-field IVT threshold value varies spatially and temporally as the underlying mean and seasonal cycle from which the anomalies are calculated vary spatially and/or temporally. Figure A1 depicts the seasonal mean comparable, or equivalent, full IVT values associated with the static anomaly detection threshold for two contrasting 3-month seasons. The basinwide mean values in Fig. A1 are approximately 475 and  $550 \text{ kg m}^{-1} \text{ s}^{-1}$  for DJF and JJA, respectively. A direct comparison of threshold values between this and other algorithms is complicated by the use of IVT anomaly fields in this approach. However, it is clear from Fig. A1 that the  $250 \text{ kg m}^{-1} \text{ s}^{-1}$  anomaly threshold cannot be considered as equivalent to a  $250 \text{ kg m}^{-1} \text{ s}^{-1}$  full-field IVT threshold for the majority of periods and locations. An alternative percentile-based threshold approach may produce results that are similar to this anomaly method, provided the distributions from which the percentiles are calculated are allowed to vary spatially and temporally.

To emphasize large-scale features, those features encompassing less than 150 contiguous grid points on the MERRA  $1/2^\circ \times 2/3^\circ$  grid are removed. The remaining anomalous IVT features are then labeled and retained for individual assessment. Characteristics of each remaining feature of interest are determined using standard image processing techniques. These characteristics are passed through layered logic and thresholding in order to retain only those features of interest that exhibit AR-like characteristics. First, the length of the major axis of the feature and ratio of major axis length to minor axis length are tested, requiring a minimum of 25 grid points (approximately 1400 km, but variable based on position

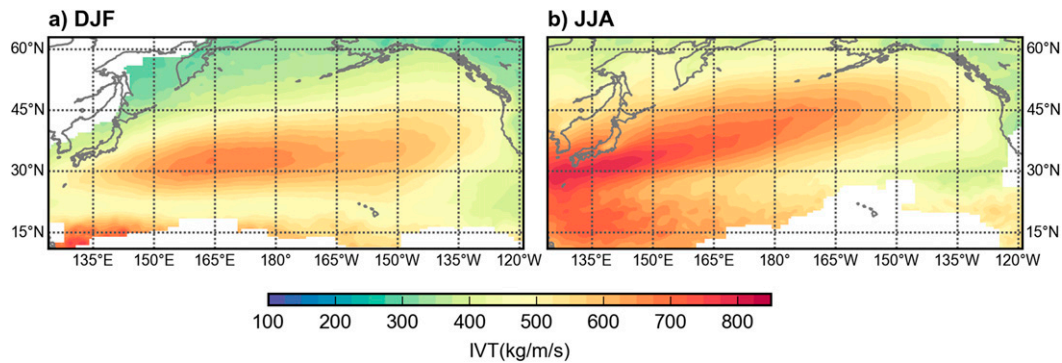


FIG. A1. Seasonal mean comparable, or equivalent, full-field IVT values associated with the static  $250 \text{ kg m}^{-1} \text{ s}^{-1}$  anomalous IVT threshold, calculated from all points along the periphery of retained AR-like features for (a) DJF and (b) JJA. Grid locations with fewer than four detected AR perimeter points are masked (white).

within the domain) and a ratio of 1.6:1, respectively, to ensure that the features are of the appropriate spatial scale and are plumelike in nature. Second, comparatively weak features with a mean anomalous IVT intensity less than  $305 \text{ kg m}^{-1} \text{ s}^{-1}$  and/or those west–east-oriented features with a center of mass equatorward of  $20^\circ\text{N}$  and orientation off the parallels of less than 0.95 radians are believed to be associated more with broad lower-frequency moisture swells and are removed. The eccentricity of a representative ellipse with the same second moments as each feature is then evaluated to eliminate those remaining features that still lack the requisite filament-like character, but were not captured by the earlier tests. The logic then assesses low-latitude features and removes those more representative of a well-developed tropical cyclone (i.e., intense circular features or features with tropical cyclone eyelike holes in the IVT anomaly field).

Features of interest that remain following the first round of logic are then evaluated to determine if multiple IVT anomaly peaks exist within each feature. The  $250 \text{ kg m}^{-1} \text{ s}^{-1}$  IVT anomaly threshold is conservative by design, but does occasionally result in “connected” anomalous IVT features, a subsection of which may be an actual AR. If multiple IVT anomaly peaks exist within a feature, the feature is segmented surrounding the peaks and then each segment’s eccentricity, mean intensity, and orientation are scrutinized for possible removal. These segmented features are flagged within the archive to afford a straightforward and deliberate inclusion or exclusion of these features during AR analyses.

Approximately 66% of the features identified in the 36-yr MERRA dataset are retained by this detection methodology. Figure A2 displays an example of the ability of the algorithm to detect AR features for an individual period. The majority of eliminated features are removed early in the algorithm because of their dimensions (e.g., too small in size or too low of a

length–width aspect ratio). Varying the static thresholds within reasonable limits slightly impacts the total number of retained features by 1%–3%. Furthermore, the order of the logical tests has little impact on the outcome of the overall algorithm, suggesting a fair amount of overlap among the series of logic tests and that no individual test is sufficient to eliminate all non-AR features.

In an effort to create a robust detection scheme that is applicable across the entire basin and all seasons, the static thresholds employed are more numerous, but perhaps not as stringent as those described in studies with more focused spatial and temporal scales (i.e., ARs making landfall along the U.S. West Coast during boreal winter). A manual review of a subset of detected features suggests that the thresholds used here are viable and important to provide a basinwide, year-round view of ARs, while still predominantly capturing significant filament-like regions of water vapor transport. As much of the imbedded logic relates to discerning ARs from tropical features in the lower latitudes of the domain (see code for details), several logic tests could be eliminated for a domain that does not extend into the tropics.

### c. Performance and yield

There exists no real, objective way to score this algorithm short of a manual comparison over the entire period of interest; however, such an approach is unreasonable—and arguably unnecessary—to facilitate these climatological analyses. Instead, a panel-by-panel visual comparison between the output and satellite imagery was performed for a random subset of the periods and facilitated the tuning of the static thresholds. For example, the  $250 \text{ kg m}^{-1} \text{ s}^{-1}$  threshold was observed to reliably outline the characteristic filamentary extent of ARs in the dataset, whereas a higher initial threshold often only captured the most intense region within each AR,



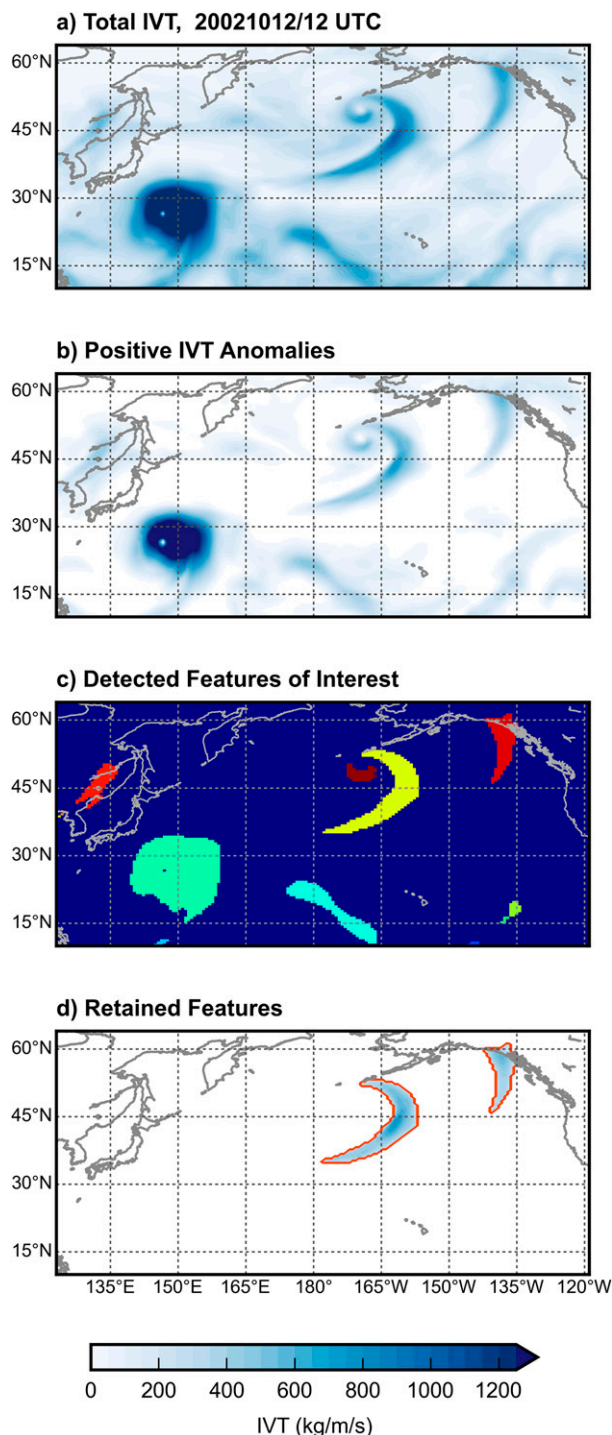


FIG. A2. An example of the ability of the algorithm to detect AR-like features in MERRA-based output from 1200 UTC 12 Oct 2002: (a) total IVT, (b) positive IVT anomalies, (c) detected features of interest, and (d) retained features.

thereby reducing the spatial expanse of the identified features. Visual inspection suggests that the vast majority of the retained features—even those near the periphery of the domain—are indeed filament-like, focused regions of water vapor transport.

Running the detection algorithm over the entire 36-yr record at 6-h resolution results in 84 462 features identified as possible ARs, the centers of mass of which fall within the defined North Pacific domain. For the results presented in section 3, the aforementioned segmented features with multiple IVT anomaly peaks are excluded, reducing the total number of AR features available for analysis to 81 409. The omission of the 3053 segmented features has little impact on the depicted composites and no bearing on the conclusions. In addition to the information regarding the time of occurrence and location of each AR, the detection algorithm also provides information regarding each feature's character, to include approximations of feature length, width, orientation, anomalous water vapor flux, etc.

#### REFERENCES

- Arkin, P. A., 1982: The relationship between interannual variability in the 200 mb tropical wind field and the Southern Oscillation. *Mon. Wea. Rev.*, **110**, 1393–1404, doi:[10.1175/1520-0493\(1982\)110<1393:TRBIVI>2.0.CO;2](https://doi.org/10.1175/1520-0493(1982)110<1393:TRBIVI>2.0.CO;2).
- Bao, J.-W., S. A. Michelson, P. J. Neiman, F. M. Ralph, and J. M. Wilczak, 2006: Interpretation of enhanced integrated water vapor bands associated with extratropical cyclones: Their formation and connection to tropical moisture. *Mon. Wea. Rev.*, **134**, 1063–1080, doi:[10.1175/MWR3123.1](https://doi.org/10.1175/MWR3123.1).
- Barnes, E. A., and L. M. Polvani, 2013: Response of the midlatitude jets, and of their variability, to increased greenhouse gases in the CMIP5 models. *J. Climate*, **26**, 7117–7135, doi:[10.1175/JCLI-D-12-00536.1](https://doi.org/10.1175/JCLI-D-12-00536.1).
- Branstator, G., 2014: Long-lived response of the midlatitude circulation and storm tracks to pulses of tropical heating. *J. Climate*, **27**, 8809–8826, doi:[10.1175/JCLI-D-14-00312.1](https://doi.org/10.1175/JCLI-D-14-00312.1).
- Capotondi, A., and Coauthors, 2015: Understanding ENSO diversity. *Bull. Amer. Meteor. Soc.*, **96**, 921–938, doi:[10.1175/BAMS-D-13-00117.1](https://doi.org/10.1175/BAMS-D-13-00117.1).
- Cordeira, J. M., F. M. Ralph, and B. J. Moore, 2013: The development and evolution of two atmospheric rivers in proximity to western North Pacific tropical cyclones in October 2010. *Mon. Wea. Rev.*, **141**, 4234–4255, doi:[10.1175/MWR-D-13-00019.1](https://doi.org/10.1175/MWR-D-13-00019.1).
- Dacre, H. F., P. A. Clark, O. Martinez-Alvarado, M. A. Stringer, and D. A. Lavers, 2015: How do atmospheric rivers form? *Bull. Amer. Meteor. Soc.*, **96**, 1243–1255, doi:[10.1175/BAMS-D-14-00031.1](https://doi.org/10.1175/BAMS-D-14-00031.1).
- Dettinger, M. D., 2013: Atmospheric rivers as drought busters on the U.S. West Coast. *J. Hydrometeor.*, **14**, 1721–1732, doi:[10.1175/JHM-D-13-02.1](https://doi.org/10.1175/JHM-D-13-02.1).
- , F. M. Ralph, T. Das, P. J. Neiman, and D. R. Cayan, 2011: Atmospheric rivers, floods, and the water resources of California. *Water*, **3**, 445–478, doi:[10.3390/w3020445](https://doi.org/10.3390/w3020445).

- Gimeno, L., R. Nieto, M. Vázquez, and D. A. Lavers, 2014: Atmospheric rivers: A mini-review. *Front. Earth Sci.*, **2**, 2.1–2.6, doi:[10.3389/feart.2014.00002](https://doi.org/10.3389/feart.2014.00002).
- Guan, B., and D. E. Waliser, 2015: Detection of atmospheric rivers: Evaluation and application of an algorithm for global studies. *J. Geophys. Res. Atmos.*, **120**, 12 514–12 535, doi:[10.1002/2015JD024257](https://doi.org/10.1002/2015JD024257).
- , —, N. P. Molotch, E. J. Fetzer, and P. J. Neiman, 2012: Does the Madden–Julian oscillation influence wintertime atmospheric rivers and snowpack in the Sierra Nevada? *Mon. Wea. Rev.*, **140**, 325–342, doi:[10.1175/MWR-D-11-00087.1](https://doi.org/10.1175/MWR-D-11-00087.1).
- , N. P. Molotch, D. E. Waliser, E. J. Fetzer, and P. J. Neiman, 2013: The 2010/2011 snow season in California's Sierra Nevada: Role of atmospheric rivers and modes of large-scale variability. *Water Resour. Res.*, **49**, 6731–6743, doi:[10.1002/wrcr.20537](https://doi.org/10.1002/wrcr.20537).
- Higgins, R. W., J.-K. E. Schemm, W. Shi, and A. Leetmaa, 2000: Extreme precipitation events in the western United States related to tropical forcing. *J. Climate*, **13**, 793–820, doi:[10.1175/1520-0442\(2000\)013<0793:EPEITW>2.0.CO;2](https://doi.org/10.1175/1520-0442(2000)013<0793:EPEITW>2.0.CO;2).
- Hoerling, M. P., and A. Kumar, 2002: Atmospheric response patterns associated with tropical forcing. *J. Climate*, **15**, 2184–2203, doi:[10.1175/1520-0442\(2002\)015<2184:ARPAWT>2.0.CO;2](https://doi.org/10.1175/1520-0442(2002)015<2184:ARPAWT>2.0.CO;2).
- Horel, J. D., and J. M. Wallace, 1981: Planetary-scale atmospheric phenomena associated with the Southern Oscillation. *Mon. Wea. Rev.*, **109**, 813–829, doi:[10.1175/1520-0493\(1981\)109<0813:PSAPAW>2.0.CO;2](https://doi.org/10.1175/1520-0493(1981)109<0813:PSAPAW>2.0.CO;2).
- Hoskins, B. J., and D. J. Karoly, 1981: The steady linear response of a spherical atmosphere to thermal and orographic forcing. *J. Atmos. Sci.*, **38**, 1179–1196, doi:[10.1175/1520-0469\(1981\)038<1179:TSLROA>2.0.CO;2](https://doi.org/10.1175/1520-0469(1981)038<1179:TSLROA>2.0.CO;2).
- Kim, H.-M., and M. A. Alexander, 2015: ENSO's modulation of water vapor transport over the Pacific–North American region. *J. Climate*, **28**, 3846–3856, doi:[10.1175/JCLI-D-14-00725.1](https://doi.org/10.1175/JCLI-D-14-00725.1).
- Knippertz, P., and H. Wernli, 2010: A Lagrangian climatology of tropical moisture exports to the Northern Hemispheric extratropics. *J. Climate*, **23**, 987–1003, doi:[10.1175/2009JCLI3333.1](https://doi.org/10.1175/2009JCLI3333.1).
- , —, and G. Gläser, 2013: A global climatology of tropical moisture. *J. Climate*, **26**, 3031–3045, doi:[10.1175/JCLI-D-12-00401.1](https://doi.org/10.1175/JCLI-D-12-00401.1).
- Lavers, D. A., and G. Villarini, 2013: The nexus between atmospheric rivers and extreme precipitation across Europe. *Geophys. Res. Lett.*, **40**, 3259–3264, doi:[10.1002/grl.50636](https://doi.org/10.1002/grl.50636).
- , —, R. P. Allan, E. F. Wood, and A. J. Wade, 2012: The detection of atmospheric rivers in atmospheric reanalyses and their links to British winter floods and the large-scale climatic circulation. *J. Geophys. Res.*, **117**, D20106, doi:[10.1029/2012JD018027](https://doi.org/10.1029/2012JD018027).
- , R. P. Allan, G. Villarini, B. Lloyd-Hughes, D. J. Brayshaw, and A. J. Wade, 2013: Future changes in atmospheric rivers and their implications for winter flooding in Britain. *Environ. Res. Lett.*, **8**, 034010, doi:[10.1088/1748-9326/8/3/034010](https://doi.org/10.1088/1748-9326/8/3/034010).
- Maloney, E. D., and M. J. Dickinson, 2003: The intraseasonal oscillation and the energetics of summertime tropical western North Pacific synoptic-scale disturbances. *J. Atmos. Sci.*, **60**, 2153–2168, doi:[10.1175/1520-0469\(2003\)060<2153:TIOATE>2.0.CO;2](https://doi.org/10.1175/1520-0469(2003)060<2153:TIOATE>2.0.CO;2).
- Matthews, A. J., 2004: Atmospheric response to observed intraseasonal tropical sea surface temperature anomalies. *Geophys. Res. Lett.*, **31**, L14107, doi:[10.1029/2004GL020474](https://doi.org/10.1029/2004GL020474).
- Nayak, M. A., G. Villarini, and D. A. Lavers, 2014: On the skill of numerical weather prediction models to forecast atmospheric rivers over the central United States. *Geophys. Res. Lett.*, **41**, 4354–4362, doi:[10.1002/2014GL060299](https://doi.org/10.1002/2014GL060299).
- Neiman, P. J., F. M. Ralph, G. A. Wick, J. D. Lundquist, and M. D. Dettinger, 2008: Meteorological characteristics and overland precipitation impacts of atmospheric rivers affecting the west coast of North America based on eight years of SSM/I satellite observations. *J. Hydrometeorol.*, **9**, 22–47, doi:[10.1175/2007JHM855.1](https://doi.org/10.1175/2007JHM855.1).
- Newell, R. E., and Y. Zhu, 1994: Tropospheric rivers: A one-year record and possible application to ice core data. *Geophys. Res. Lett.*, **21**, 113–116, doi:[10.1029/93GL03113](https://doi.org/10.1029/93GL03113).
- , N. E. Newell, Y. Zhu, and C. Scott, 1992: Tropospheric rivers?—A pilot study. *Geophys. Res. Lett.*, **19**, 2401–2404, doi:[10.1029/92GL02916](https://doi.org/10.1029/92GL02916).
- Newman, M., G. N. Kiladis, K. M. Weickmann, F. M. Ralph, and P. D. Sardeshmukh, 2012: Relative contributions of synoptic and low-frequency eddies to time-mean atmospheric moisture transport, including the role of atmospheric rivers. *J. Climate*, **25**, 7341–7360, doi:[10.1175/JCLI-D-11-00665.1](https://doi.org/10.1175/JCLI-D-11-00665.1).
- Payne, A. E., and G. Magnusdottir, 2014: Dynamics of landfalling atmospheric rivers over the North Pacific in 30 years of MERRA reanalysis. *J. Climate*, **27**, 7133–7150, doi:[10.1175/JCLI-D-14-00034.1](https://doi.org/10.1175/JCLI-D-14-00034.1).
- Ralph, F. M., P. J. Neiman, and G. A. Wick, 2004: Satellite and CALJET aircraft observations of atmospheric rivers over the eastern North Pacific Ocean during the winter of 1997/98. *Mon. Wea. Rev.*, **132**, 1721–1745, doi:[10.1175/1520-0493\(2004\)132<1721:SACAOO>2.0.CO;2](https://doi.org/10.1175/1520-0493(2004)132<1721:SACAOO>2.0.CO;2).
- , —, S. I. Gutman, M. D. Dettinger, D. R. Cayan, and A. B. White, 2006: Flooding on California's Russian River: Role of atmospheric rivers. *Geophys. Res. Lett.*, **33**, L13801, doi:[10.1029/2006GL026689](https://doi.org/10.1029/2006GL026689).
- , —, G. N. Kiladis, K. Weickmann, and D. W. Reynolds, 2011: A multiscale observational case study of a Pacific atmospheric river exhibiting tropical/extratropical connections and a mesoscale frontal wave. *Mon. Wea. Rev.*, **139**, 1169–1189, doi:[10.1175/2010MWR3596.1](https://doi.org/10.1175/2010MWR3596.1).
- , T. Coleman, P. J. Neiman, R. J. Zamora, and M. D. Dettinger, 2013: Observed impacts of duration and seasonality of atmospheric-river landfalls on soil moisture and runoff in coastal Northern California. *J. Hydrometeorol.*, **14**, 443–459, doi:[10.1175/JHM-D-12-076.1](https://doi.org/10.1175/JHM-D-12-076.1).
- Riehl, H., T. C. Yeh, and N. E. La Seur, 1950: A study of variations of the general circulation. *J. Meteor.*, **7**, 181–194, doi:[10.1175/1520-0469\(1950\)007<0181:ASOVOT>2.0.CO;2](https://doi.org/10.1175/1520-0469(1950)007<0181:ASOVOT>2.0.CO;2).
- Rienecker, M. M., and Coauthors, 2011: MERRA: NASA's Modern-Era Retrospective Analysis for Research and Applications. *J. Climate*, **24**, 3624–3648, doi:[10.1175/JCLI-D-11-00015.1](https://doi.org/10.1175/JCLI-D-11-00015.1).
- Ryoo, J.-M., Y. Kaspi, D. W. Waugh, G. N. Kiladis, D. E. Waliser, E. J. Fetzer, and J. Kim, 2013: Impact of Rossby wave breaking on U.S. West Coast winter precipitation during ENSO events. *J. Climate*, **26**, 6360–6382, doi:[10.1175/JCLI-D-12-00297.1](https://doi.org/10.1175/JCLI-D-12-00297.1).
- Sampe, T., and S.-P. Xie, 2010: Large-scale dynamics of the meiyu-baiu rainband: Environmental forcing by the westerly jet. *J. Climate*, **23**, 113–134, doi:[10.1175/2009JCLI3128.1](https://doi.org/10.1175/2009JCLI3128.1).
- Smith, T. M., R. W. Reynolds, T. C. Peterson, and J. Lawrimore, 2008: Improvements to NOAA's historical merged land–ocean surface temperature analysis (1880–2006). *J. Climate*, **21**, 2283–2296, doi:[10.1175/2007JCLI2100.1](https://doi.org/10.1175/2007JCLI2100.1).
- Sodemann, H., and A. Stohl, 2013: Moisture origin and meridional transport in atmospheric rivers and their association with multiple cyclones. *Mon. Wea. Rev.*, **141**, 2850–2868, doi:[10.1175/MWR-D-12-00256.1](https://doi.org/10.1175/MWR-D-12-00256.1).
- Waliser, D. E., and Coauthors, 2012: The “year” of tropical convection (May 2008–April 2010): Climate variability and

- weather highlights. *Bull. Amer. Meteor. Soc.*, **93**, 1189–1218, doi:[10.1175/2011BAMS3095.1](https://doi.org/10.1175/2011BAMS3095.1).
- Warner, M. D., C. F. Mass, and E. P. Salathé Jr., 2012: Wintertime extreme precipitation events along the Pacific Northwest coast: Climatology and synoptic evolution. *Mon. Wea. Rev.*, **140**, 2021–2043, doi:[10.1175/MWR-D-11-00197.1](https://doi.org/10.1175/MWR-D-11-00197.1).
- , —, and —, 2015: Changes in winter atmospheric rivers along the North American west coast in CMIP5 climate models. *J. Hydrometeor.*, **16**, 118–128, doi:[10.1175/JHM-D-14-0080.1](https://doi.org/10.1175/JHM-D-14-0080.1).
- Wheeler, M. C., and H. H. Hendon, 2004: An all-season real-time multivariate MJO index: Development of an index for monitoring and prediction. *Mon. Wea. Rev.*, **132**, 1917–1932, doi:[10.1175/1520-0493\(2004\)132<1917:AARMMI>2.0.CO;2](https://doi.org/10.1175/1520-0493(2004)132<1917:AARMMI>2.0.CO;2).
- Wick, G. A., P. J. Neiman, and F. M. Ralph, 2013: Description and validation of an automated objective technique for identification and characterization of the integrated water vapor signature of atmospheric rivers. *IEEE Trans. Geosci. Remote Sens.*, **51**, 2166–2176, doi:[10.1109/TGRS.2012.2211024](https://doi.org/10.1109/TGRS.2012.2211024).
- Woollings, T., A. Hannachi, and B. Hoskins, 2010: Variability of the North Atlantic eddy-driven jet stream. *Quart. J. Roy. Meteor. Soc.*, **136**, 856–868, doi:[10.1002/qj.625](https://doi.org/10.1002/qj.625).
- Zhu, Y., and R. E. Newell, 1994: Atmospheric rivers and bombs. *Geophys. Res. Lett.*, **21**, 1999–2002, doi:[10.1029/94GL01710](https://doi.org/10.1029/94GL01710).
- , and —, 1998: A proposed algorithm for moisture fluxes from atmospheric rivers. *Mon. Wea. Rev.*, **126**, 725–735, doi:[10.1175/1520-0493\(1998\)126<0725:APAFMF>2.0.CO;2](https://doi.org/10.1175/1520-0493(1998)126<0725:APAFMF>2.0.CO;2).